Chapter 21
Syntheses of Composite Porous Materials for Solid Oxide Fuel Cells

Hiroya Abe and Kazuyoshi Sato

Abstract This section focuses on the syntheses and characterization of composite porous materials for solid oxide fuel cell (SOFC) electrodes. Considerable efforts have been made to enlarge the triple phase boundary (TPB) where electrode, electrolyte, and pore phases meet, for reducing polarization loss in SOFC. Composite particles, which consist of electrode and electrolyte materials, have been prepared for this purpose, because their utilization is to improve the homogeneity of electrode and electrolyte particle distribution in SOFC electrodes. Among several wet-chemical routes for syntheses of the composite particles, coprecipitation method has been found a particular interest because of its simplicity, cost-effective, and easy scale-up capability. The emphasis will be therefore placed on the development of coprecipitation methods for enlarged TPB in SOFC electrodes.

Keywords Solid oxide fuel cells · Triple phase boundary · Coprecipitation · Composite particle · Structural control

21.1 Introduction

Fuel cells are considered highly efficient devices to convert chemical energy directly into electrical energy with low emission of pollutants [1]. Among the several types of fuel cells, solid oxide fuel cells (SOFCs) can achieve highest efficiency, due to their high operation temperature such as 1000 °C. In the past several decades, the development of SOFCs has been made significant progress, resulting in an increase of power density [1].
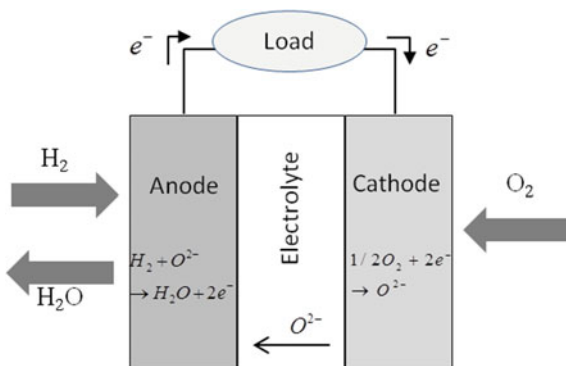
H. Abe (✉)
Joining and Welding Research Institute, Osaka University,
11-1 Mihogaoka, Ibaraki, Osaka 567-0047, Japan
e-mail: h-abe@jwri.osaka-u.ac.jp

K. Sato
Graduate School of Science & Technology, Gunma University,
1-5-1 Tenjin-cho, Kiryu, Gunma 376-8515, Japan

SOFCs are composed of a porous cermet anode and a porous oxide cathode, with a dense electrolyte sandwiched by them (see Fig. 21.1). Typically, air is fed to the cathode as an oxygen source, and fuel including H_2, CO, and CH_4 is fed to the anode. When oxygen gas contacts the cathode/electrolyte interface, the oxygen molecules are electrochemically reduced to form oxygen ions (O^{2-}). These oxygen ions are moved through the electrolyte to the anode, where they electrochemically oxidize the fuel. As the fuel is oxidized, the electrons are released with a higher potential to an external circuit, thus providing power [2]. State-of-the-art SOFCs are composed of yttria-stabilized zirconia (YSZ) electrolyte, Ni–YSZ cermet anode, and a lanthanum–strontium–manganite (LSM) cathode [3].

Recent development on SOFCs have been paid much attention to reduce the operating temperature into the so-called intermediate range (600–800 °C), with the aim of cost reduction and durability enhancement of the cells and the system [4]. However, when the temperature decreases, a significant increase in not only electrolyte ohmic resistance but also polarization resistances of both electrodes is observed [1, 3].

To reduce the electrolyte ohmic resistance at the temperature range, a thin-film electrolyte configuration has been proposed since the resistance is proportional to the thickness [5]. As shown in Fig. 21.2, conventional ceramics powder processing such as tape casting and screen printing has been applied in the fabrication of the thin-film electrolyte SOFCs, i.e., anode or cathode supported SOFCs. The thicknesses down to 10 μm have been successfully achieved and probed to exhibit excellent electrochemical performance [5]. Another significant contribution is the polarization resistance of the electrodes. In case of Ni–YSZ cermet anode [6], the reaction rate for electrochemical oxidation of hydrogen is correlated with the length of the triple phase boundary (TPB) where Ni, YSZ, and pore phases meet as shown in Fig. 21.3. In case of LSM–YSZ cathode, it has been also reported that the oxygen reduction reaction occurs in the vicinity of TPB [7]. These indicate that making extension of the TPB is a technological aim for the reduction of polarization loss.
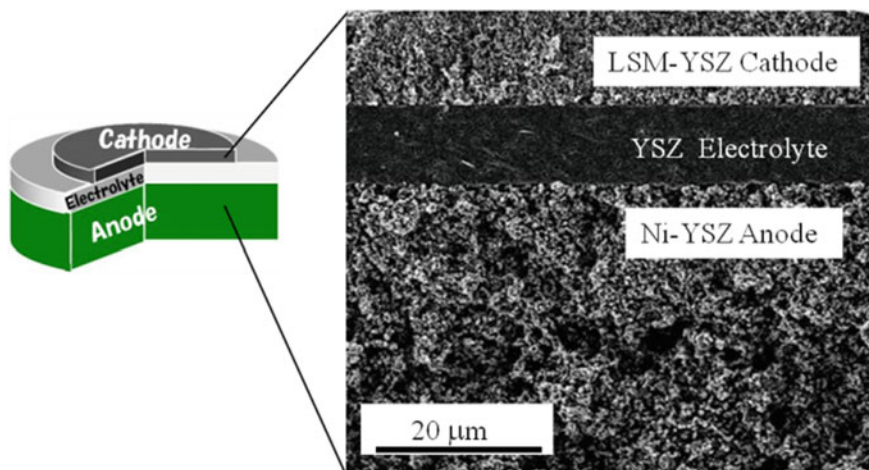
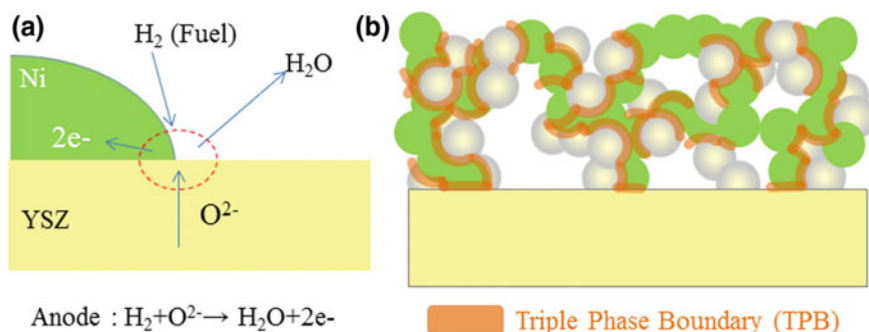**Fig. 21.2** Cross sectional view of an anode-supported SOFC

Fig. 21.3 Schematic diagrams of **a** electrochemical reaction at Ni–YSZ anode and **b** triple phase boundary formed in Ni–YSZ composite porous layer

Considerable efforts have been made to enlarge the TPB by controlling the composite microstructure of SOFC electrodes [8, 9]. The previous studies have used the ball-milling technique and determined that the important parameters are the particle diameter, powder size distribution, electrode/electrolyte particles compounding ratio and the degree of calcinations. These control parameters, however, have complicated optimization of the electrode microstructure.

In addition to the conventional mechanical mixing of the electrode (NiO or LSM) and the electrolyte (YSZ) particles, their composite particles can be directly synthesized by wet chemical routes. The purpose of the direct synthesis is primarily to improve the homogeneity of electrode and electrolyte phase distribution and thereby to increase electrode performances. Polymeric complexing [10–12], spray pyrolysis [13–15], and coprecipitation methods [16–18] have been proved to be a

good synthesize route for the preparation of composite particles. Among these routes, the coprecipitation method has been found particular interest because of its simplicity, cost-effective, and easy scale-up capability. In this section, therefore, the emphasis will be placed on the development of coprecipitation methods for SOFC electrodes.

21.2 Precipitation of Metal Hydroxides

The most common method used to collect soluble metal ions from a solution is to precipitate the species as a metal hydroxide. By raising the pH value of the solution, the corresponding metal hydroxides become insoluble and precipitate from solution. First, it is important to understand the precipitation behavior of the metal hydroxides from the solubility curves [19]. The precipitation of metal hydroxide $M(OH)_n$ can be described as

$$M^{n+} + n(OH)^- \rightarrow M(OH)_n \tag{21.1}$$
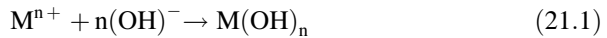
where n is the valence of metal ion in the solution. The solubility product K_{SP} of $M(OH)_n$ is

$$K_{SP} = [M^{n+}][OH^-]^n \tag{21.2}$$

$$\log K_{SP} = \log[M^{n+}] + n \cdot \log[OH^-] \tag{21.3}$$

$[M^{n+}]$ and $[OH^-]$ were the mole concentration of M^{n+} and OH^- in the solution, respectively. The ionic product of water at 25 °C under the ambient pressure is $10^{-14} M^2$.

$$-\log[H^+] - \log[OH] = pH + pOH = 14 \tag{21.4}$$

Therefore Eq. (21.3) can be described as follows:

$$\log K_{SP} = \log[M^{n+}] - 14n - n\log[H^+] \tag{21.5}$$

$$\log[M^{n+}] = -\log K_{SP} + 14n - npH \tag{21.6}$$

K_{sp} can be obtained from the literature [20, 21]. For example, Fig. 21.4 shows the solubility curves of $Zr(OH)_4$, $Y(OH)_3$ and $Ni(OH)_2$ as a function of pH. Metal ion (M^{n+}) is stable (unsaturated state) in the left side of the curve, while metal hydroxide $M(OH)_n$ is stable (supersaturated state) in the right side.

The pH value of a solution is controlled using an alkaline solution such as NaOH or NH_3. Typically, the alkaline solution is dropped into the acid solution of the component cations to obtain the precipitates, which is called as "normal sequence".

Fig. 21.4 Solubility of Zr $(OH)_4$, $Y(OH)_3$, and $Ni(OH)_2$ as a function of pH at 25 °C. Reprinted from Ref. [19], Copyright 2009 with permission from Elsevier
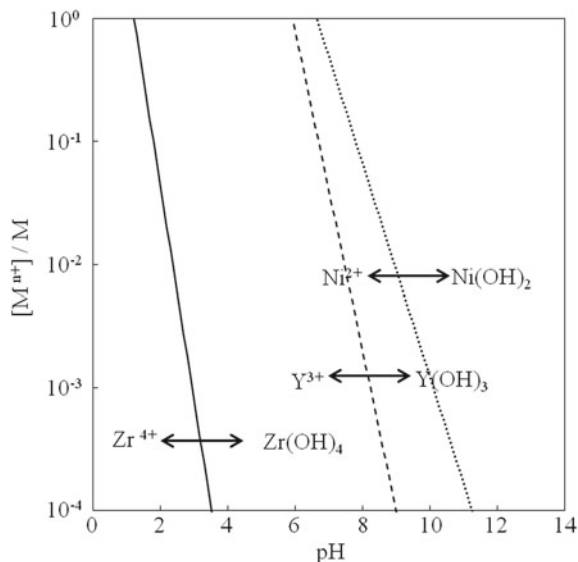
When the normal sequence is used for the solution dissolved with Zr^{4+}, Y^{3+}, and Ni^{2+}, $Zr(OH)_4$ precipitates first, then $Y(OH)_3$ and $Ni(OH)_2$ precipitate from the solubility curves as shown in Fig. 21.4. As a result, the precipitates would be not homogenous.

21.3 Coprecipitation Under Reverse Sequence

There is an alternative sequence. The mixed cation solution is dropped into the alkaline solution (reservoir). The reservoir pH can be kept constant by adding the extra alkaline solution. The pH in the local region undergoes a change near the droplet, presenting the smaller precipitation system compared to the normal sequence.

The coprecipitation under the reverse sequence has been investigated by the authors for synthesizing NiO–YSZ composite particles [19]. Figure 21.5 shows the effect of reservoir pH on the morphology of the composite particles. The samples synthesized at pH 10 and pH 11 contained very large NiO grains (see Fig. 21.5b, c). On the other hand, the nanocomposite particles were synthesized at pH 13 (see Fig. 21.5d). The clear difference of the microstructure depending on the reservoir pH can be attributed to the difference of nucleation density and growth of the hydroxides. When the reservoir pH was the highest, the number density of nuclei increases and the difference of precipitation rate among $Zr(OH)_4$, $Y(OH)_3$ and $Ni(OH)_2$ decreases. As a consequence, the fine hydroxide phases with uniform distribution could be obtained at pH 13. The uniformly distributed NiO and YSZ
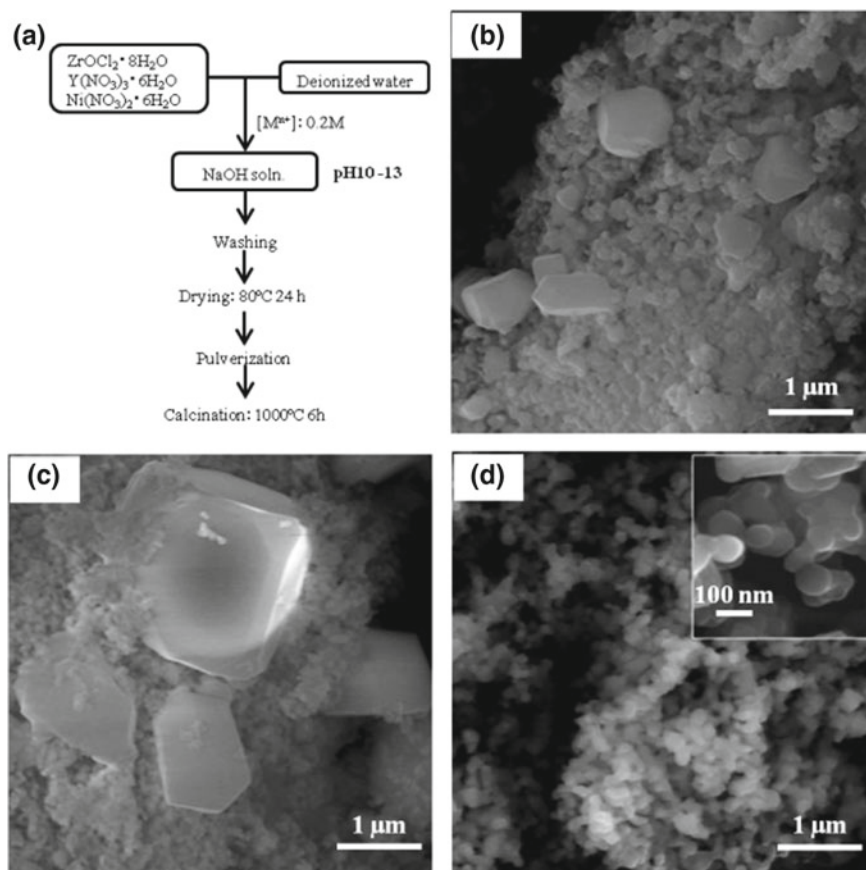
Fig. 21.5 **a** Synthetic flowchart and scanning electron microscopy (SEM) images of the NiO/YSZ composite particles synthesized at **b** pH 10, **c** pH 11, and **d** pH 13. Modified from Ref. [19], Copyright 2009 with permission from Elsevier

phases suppressed the grain growth each other during the subsequent calcination step, resulting in a successful synthesis of the NiO/YSZ nanocomposite particles at pH 13.

The anode was fabricated by screen printing of the paste consisting of the NiO/YSZ composite particles and polyethylene glycol followed by sintering at 1300 °C for 2 h. Finally, the Ni–YSZ cermet anode was obtained by reducing with H_2 + 3% H_2O at 800 °C. The composite particles synthesized at pH 10 resulted in coarse and inhomogeneous anode microstructure and moderate area specific resistance (ASR) as 0.57 Ω cm^2 at 800 °C under open-circuit voltage (OCV). Contrarily, the nanocomposite particles synthesized at pH 13 provided fine as well as homogeneous porous microstructure with the grain size in the range 200–400 nm and the lower ASR as 0.36 Ω cm^2 at 800 °C under OCV.

The nanocomposite particles with sodium contamination may reduce the long-term stability of the anode [22]. Tetramethylammonium hydroxide (TMAH, $(CH_3)_4NOH$) is another choice to keep the high pH in the reverse titration method.

21.4 Coprecipitation in YSZ Nanocrystal Sol

Recently, reliable and reproducible methods have been developed for preparing large quantities of inorganic nanocrystals. Aqueous sols containing the inorganic nanocrystals have been also available. Here, a unique coprecipitation method using an aqueous sol of YSZ nanocrystal is shown for the synthesis of NiO–YSZ nanocomposite particles [23].

The aqueous sol used in our experiment was the colloid containing YSZ nanocrystals (Sumitomo Osaka Cement Co. Ltd., Japan). The sol has a highly transparent appearance due to superior dispersion (almost no agglomeration) as shown in the left of Fig. 21.6a. The dynamic light scattering revealed that the nanocrystals had a narrow size distribution with an average diameter of 3 nm (Fig. 21.6b), showing good agreement with that observed in transmission electron microscopy (TEM) image.

The specific feature of the YSZ sol is its well-dispersed ability even in the highly concentrated metal salts (nitrate and chloride) solution. In the present case, a Ni$(NO_3)_2 \cdot 6H_2O$ was dissolved to be the total concentration of YSZ and Ni$(NO_3)_2 \cdot 6H_2O$ is 0.2 M. After the dissolving, the sol maintained transparency, indicating that the YSZ nanoparticles preserved their well-dispersed state as shown in the right of Fig. 21.6a. Although the origin of YSZ nanocrystal dispersion in a relatively high salt has not been clarified yet, it would be probably hydration force (non-DLVO force [24]).

The YSZ–Ni^{2+} mixed solution was dropped into NH_4HCO_3 solution at room temperature. During the coprecipitation, NH_3 solution (Wako Chemicals, Japan) was added simultaneously into NH_4HCO_3 solution to keep the pH at 8. The corresponding Ni compound (approximately $Ni(CO_3)_{2/3}(OH)_{2/3} \cdot nH_2O$), was deposited on YSZ nanocrystals and coprecipitated. The crystalline YSZ nanoparticles (in the circles) were uniformly distributed entire the noncrystalline Ni compound phase (Fig. 21.6c) in the precipitates. Organic bases such as tetramethylammonium hydrogen carbonate solution (TMAC, $(CH_3)_4NHCO_3$) and TMAH is available as the alkaline solutions. Since Ni ion does not form any soluble complexes with them, more precise control of NiO–YSZ mixing ratio can be possible.

Both YSZ and NiO phases were identified in the X-ray diffraction profile for the sample calcined at 600 °C. Their average crystalline sizes, estimated by Scherrer's formula, were about 6 and 4 nm, respectively. Also, the HRTEM image evidenced the successful fabrication of the NiO/YSZ nanocomposite particles with the size of about 5 nm (Fig. 21.6d).

Then the anode layer was fabricated on the sintered YSZ disk from the NiO/YSZ nanocomposite particles, through screen printing followed by sintering at 1300 °C
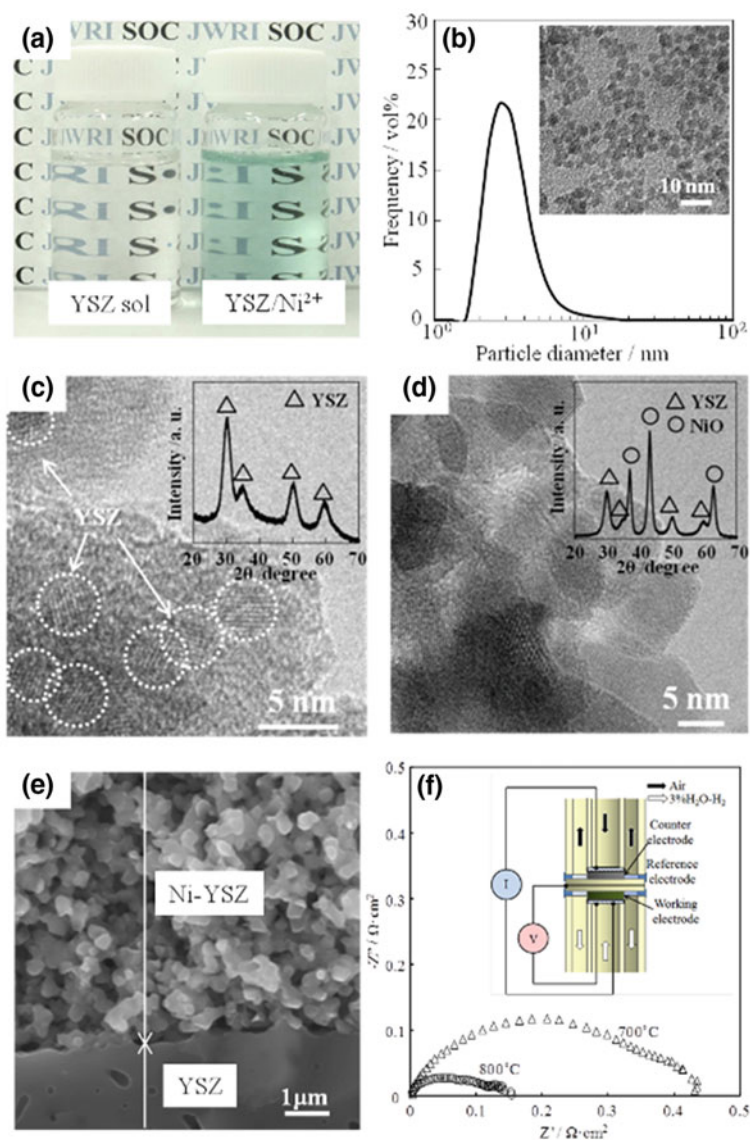
Fig. 21.6 a Appearance of aqueous sol of YSZ nanocrystals, **b** its size distribution (*inset* TEM image of the YSZ nanocrystals), **c** HRTEM image and XRD pattern of the coprecipitated sample, **d** HRTEM image XRD pattern of the NiO/YSZ nanocomposite particles calcined at 600 °C, **e** cross-sectional SEM image of the Ni/YSZ anode, **f** electrochemical impedance spectra of the Ni/YSZ anode measured at 700 and 800 °C under OCV. Modified with permission from Ref. [23], Copyright 2010 Wiley

for 2 h. Finally, the Ni–YSZ cermet anode was obtained as mentioned above. The microstructural examination reveals that the anode consisted of fine grains with the size of 200–300 nm (Fig. 21.6e). The grain size is one order of magnitude smaller than that of conventional anodes. Fine and well percolating solid and pore phases can be attributed to the homogeneous arrangement of NiO and YSZ phases in the nanocomposite particles. ASR of the anode was 0.43 and 0.15 Ω cm^2 at 700 and 800 °C, respectively (Fig. 21.6f). These values were significantly lower than those reported in the literatures on Ni/YSZ anodes [23]. It is clearly attributable to the fine composite microstructure, leading to extended adsorption sites and reduced diffusion length of hydrogen, in addition to the significantly enlarged TPB. The formation of the fine grains surely resulted from prevention of abnormal grain growth due to the homogeneously distributed two particle phases.

To estimate TBP length, the three-dimensional microstructure of an SOFC anode has been characterized using a focused ion beam–scanning electron microscope (FIB-SEM). The Ni–YSZ anode was fabricated from NiO–YSZ composite layer sintered at 1350 °C followed by reduction. The volume ratio was Ni:YSZ = 50:50. The microstructure of the anode is virtually reconstructed in a computational field using a series of acquired two dimensional SEM images (Fig. 21.7a, b). The TPB density is estimated to be ∼8 μm/μm^3 (Fig. 21.7c), which is longer than that obtained by a mechanical mixing method [25].

The LSM/YSZ nanocomposite powder was also synthesized with the similar manner [26]. Then, the fine-structured LSM/YSZ porous film has been fabricated for a cathode electrode, and it was demonstrated that the ASR was significantly reduced due to the enlarged TPB formed in the fine composite microstructure [27]. The anode-supported cell of Ni–YSZ/YSZ/LSM–YSZ was fabricated using the LSM–YSZ nanocomposite particles. The cells exhibited the high power density of 0.20, 0.40, 0.69, and 0.85 W/cm^2 at 650, 700, 750, and 800 °C, respectively, under the cell voltage of 0.7 V [27]. This high performance indicates that the anode-supported cell with the nanostructured cathode has potential to be operated at the intermediate temperature range with an acceptable power density.
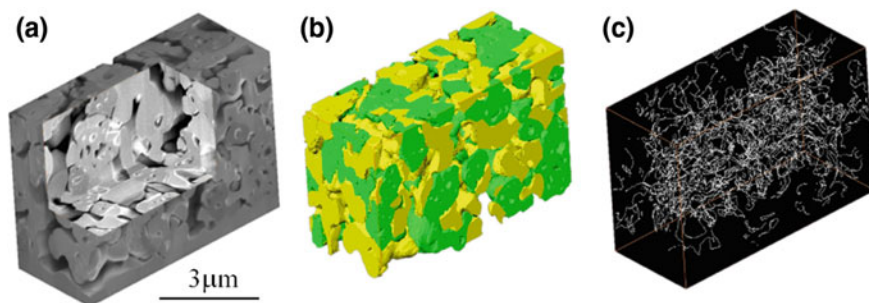

Fig. 21.7 **a** FIB-SEM image of Ni–YSZ anode from the reduction of NiO–YSZ sintered at 1350 °C, **b** 3D Ni–YSZ anode reconstruction, Ni(green) and YSZ(yellow), **c** 3D map of three-phase boundaries in the anode

21.5 Coprecipitation with Anionic Zr(IV) Complex Solution

Zr^{4+} forms soluble anionic complexes with hydroxide and carbonate ions in aqueous solution [28]. Karlysheva et al. predicted the generation of [Zr $(OH)_2(CO_3)_2]^{2-}$ in a mixed solution of $ZrOCl_2$ and Na_2CO_3 at pH > 7 [29]. Malinko et al. demonstrated the presence of $[Zr(OH)_2(CO_3)_2]^{2-}$, $[Zr(OH)(CO_3)_3]^{3-}$, and $[Zr(CO_3)_4]^{4-}$, depending on the concentration of carbonate in a mixed solution of Na_2CO_3 and $Zr(SO_4)^2$ [30]. Veyland et al. revealed a variation in the number of carbonate ions coordinating to zirconium depending on the chemical composition of a mixed solution of $K_2CO_3–KHCO_3–ZrOCl_2$ [31]. The authors have simply prepared a transparent solution of anionic Zr complex, $[Zr(OH)_2(CO_3)_2]^{2-}$, by mixing $ZrOCl_2$ and TMAC $((CH_3)_4NHCO_3)$ solutions (Fig. 21.8). The anionic Zr complex is stable in pH 7–10 at temperatures below about 80 °C.

It has been reported that the soluble anionic Zr complex can be used as the precursor for the synthesis of Zr-based materials. Afanasiev has synthesized the mesoporous ZrO_2 though reaction with cetyltrimethylammonium bromide (CTAB) [32]. The authors have synthesized monoclinic ZrO_2 [33] and YSZ nanocrystals
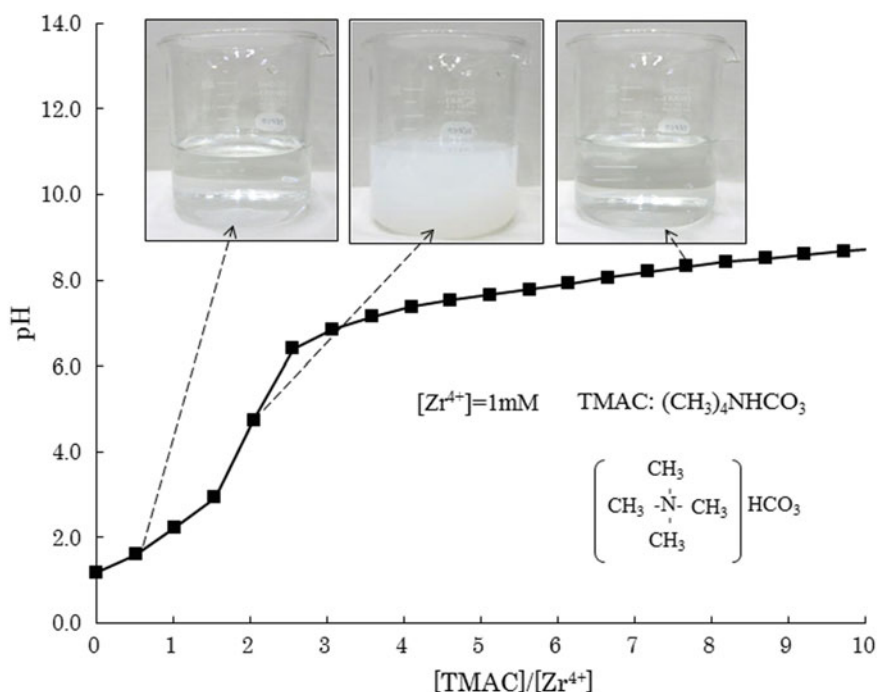

Fig. 21.8 pH titration curve for 1 mM solution of $ZrOCl_2$ under TMAC $((CH_3)_4NHCO_3)$ addition
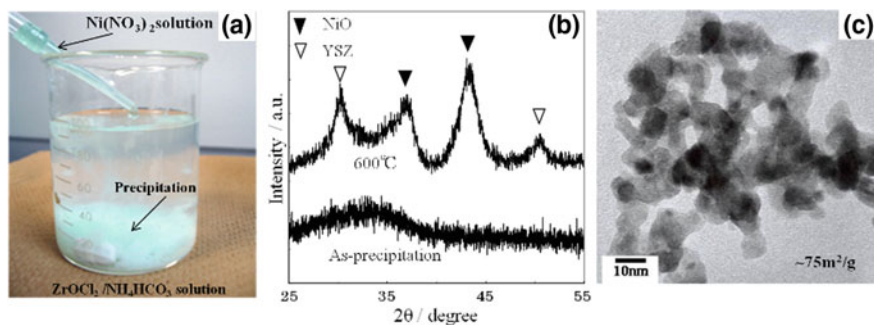
Fig. 21.9 **a** precipitation phenomenon by dropping of Ni(NO₃)₂ solution into the Zr complex solution (ZrOCl₂/NH₄HCO₃), **b** XRD patterns for the precipitate calcined at 600 °C, **c** TEM image of the sample (**b**)

[34] under hydrothermal condition with tetramethylammonium ion as capping agent. Also, an interesting coprecipitation phenomenon has been found in the soluble anionic Zr complex. Recently, highly dispersive nanocomposite particles have been synthesized based on this interesting coprecipitation [35].

Here, the synthesis of NiO–YSZ nanocomposite particles using anionic Zr complex is briefly shown. The soluble anionic Zr complex was prepared by mixing $ZrOCl_2$ and NH_4HCO_3 solutions. When Ni nitrate solution was dropped in the soluble anionic Zr complex solution, a mint-green precipitate was obtained (Fig. 21.9a). Concentrations of Ni and Zr ions in the supernatant solution were measured to be less than 5% of initial concentrations, indicating that the precipitates contained both Ni and Zr. Supplementary experiments suggested that aqua ligands in $[Ni(H_2O)_6]^{2+}$ complex play an important role on the reaction with anionic Zr complex. Similarly, a precipitation was observed when $Y(NO_3)_3$ aqueous solution is dropped, too. Therefore, when the solution of Ni and Y nitrates was dropped, the compound containing Ni, Y and Zr was easily coprecipitated. The thermal decomposition of the precipitates accompanying with the evolution of H_2O and CO_2 was almost completed until 450 °C, and no significant weight loss was observed during further increase of temperature. The XRD and TEM revealed that the products calcined at 600 °C consisted of nanosized NiO and YSZ grains (Fig. 21.9b, c), which were surely highly homogeneous.

21.6   Conclusion

Advanced coprecipitation routes have been developed to synthesize nanocomposite particles suitable for application in SOFC electrodes. The reverse sequence coprecipitation with the strong alkaline solution is a promising approach to obtain the hydroxides including $Zr(OH)_4$, $Y(OH)_3$, and $Ni(OH)_2$ with homogeneous phase

distributions, compared to conventional normal sequence. In addition, the coprecipitation with YSZ nanocrystal can produce the homogeneous precipitate for the synthesis of NiO–YSZ and LSM–YSZ nanocomposite particles. Furthermore, it is demonstrated that coprecipitation through reaction of Ni^{2+} and aqueous anionic Zr (IV) complex is another way for homogeneous NiO–YSZ nanocomposites. It is expected that there are opportunities of these facile synthetic routes for not only SOFC electrodes but also advanced composite materials.

References

1. B.C.H. Steele, A. Heinsel, Nature **414**, 345 (2001)
2. T.A. Adams, J. Nease, D. Tucker, P.I. Barton, Ind. Eng. Chem. Res. **52**, 3089 (2013)
3. S.M. Haile, Acta Mater. **51**, 5981 (2003)
4. Z. Shao, W. Zhou, Z. Zho, Prog. Mater. Sci. **57**, 804 (2012)
5. J. Will, A. Mitterdorfer, C. Kleinlogel, D. Perednis, L.J. Gaucker, Solid State Ionics **131**, 79 (2000)
6. A. Bieberle, L.P. Meier, L.J. Gauckler, J. Electrochem. Soc. **148**, A646 (2001)
7. K. Sasaki, J.P. Wurth, R. Gschwend, M. Gödickemeier, L.J. Gauckler, J. Electrochem. Soc. **143**, 530 (1996)
8. S.P. Jiang, S.H. Chan, J. Mater. Sci. **39**, 4405 (2004)
9. S.P. Jiang, J. Mater. Sci. **43**, 6799 (2008)
10. J. Martynczuk, M. Arnold, H. Wang, J. Caro, A. Feldhoff, Adv. Mater. **19**, 2134 (2007)
11. S.D. Kim, H. Moon, S.H. Hyun, J. Moon, J. Kim, H.W. Lee, Solid State Ionics **178**, 1304 (2007)
12. J.X. Wang, Y.K. Tao, J. Shao, W.G. Wang, J. Power Sources **186**, 344 (2009)
13. T. Fukui, T. Oobuchi, Y. Ikuhara, S. Ohara, K. Kodera, J. Am. Ceram. Soc. **80**, 261 (1997)
14. T. Fukui, S. Ohara, K. Mukai, Electrochem. Solid-State Lett. **1**, 120 (1998)
15. A. Hagiwara, N. Hobara, K. Takizawa, K. Sato, H. Abe, M. Naito, Solid State Ionics **178**, 1552 (2007)
16. G.M. Grgicak, R.G. Green, W.F. Du, J.B. Giorgi, J. Am. Ceram. Soc. **88**, 3081 (2005)
17. Y. Li, Y. Xie, J. Gong, Y. Chen, Z. Zhang, Mater. Sci. Eng. **B86**, 119 (2001)
18. X. Fang, G. Zhu, C. Xia, X. Liu, G. Meng, Solid State Ionics **168**, 31 (2004)
19. K. Sato, G. Okamoto, M. Naito, H. Abe, J. Power Sources **193**, 185 (2009)
20. L.G. Sillen, A.E. Martell, in *Stability Constants of Metal-Ion Complexes*, No. 17 and No. 25 (Chemical Society, London, 1964 and 1971)
21. W. Feitknecht, P. Scindler, Pure Appl. Chem. **6**, 130 (1963)
22. Y.L. Liu, S. Primdahl, M. Morgensen, Solid Sate Ionics **161**, 1 (2003)
23. K. Sato, T. Kinoshita, H. Abe, Fuel Cells **10**, 320 (2010)
24. J. Israelachvili, in *Intermolecular and Surface Forces*, 2nd edn. (Academic Press, 1991), pp. 260–282
25. J.R. Wilson, S.A. Barnett, Electrochem. Solid-State Lett. **11**, B181 (2008)
26. K. Sato, T. Kinoshita, H. Abe, M. Naito, J. Ceram. Soc. Jpn. **117**, 1186 (2009)
27. K. Sato, T. Kinoshita, H. Abe, J. Power Sources **195**, 4144 (2009)
28. F. Takahashi, K. Fujiwara, Y. Nakajima, T. Nishikawa, H. Masu, M. Imanari, Y. Hidaka, N. Ogawa, Dalton Trans. **44**, 645
29. K.F. Karlysheva, L.S. Chumakova, L.A. Malinko, I.A. Sheka, Russ. J. Inorg. Chem. **27**, 1582 (1982)
30. L.A. Malinko, L.S.C. Chumakova, K.I. Arsenin, K.F. Karlysheva, I.A. Sheka, Russ. J. Inorg. Chem. **25**, 1184 (1980)

31. A. Veyland, L. Dupont, J. Rimbault, J.C. Pierrard, M. Aplincourt, Helv. Chim. Acta **83**, 414 (2000)
32. P. Afanasiev, Mater. Res. Bull. **37**, 1933 (2002)
33. K. Sato, H. Abe, S. Ohara, J. Am. Chem. Soc. **132**, 2538 (2009)
34. K. Sato, K. Horiguchi, T. Nishikawa, S. Yagishita, K. Kuruma, T. Murakami, H. Abe, Inorg. Chem. **54**, 7976 (2015)
35. X. Xi, H. Abe, K. Kuruma, R. Harada, A. Shui, M. Naito, Adv. Powder Technol. **25**, 490 (2014)